

# A Low Side Lobe Level Parabolic Antenna for Meteorological Applications

A. Eszes<sup>1,2</sup>, Zs. Szabó<sup>1,\*</sup>, B. Ladányi-Turóczy<sup>2</sup>, and I. Kalácska<sup>2</sup>

<sup>1</sup>Pázmány Péter Catholic University, Faculty of Information Technology and Bionics, Hungary

<sup>2</sup>Grante Antenna Development and Production Co., Hungary

**ABSTRACT:** A novel corrugated subreflector is developed to achieve sufficient side lobe level suppression for antenna systems used in meteorological applications. The subreflector operates at 9.41 GHz, with a 60 MHz bandwidth and an efficiency of more than 70%. Its structure is rotational symmetric and is suitable for parabolic antenna applications. It can be utilized in single-polarized or polarimetric radar systems. The pattern-forming property of the subreflector is achieved with corrugations of different depths. Analytical design formulas have been deduced by solving the aperture integral. The analytical formulas provide the initial geometrical configuration and the reference illumination pattern in the objective function to which full-wave electromagnetic optimizations are performed to obtain the final corrugation depths. The subreflector has been manufactured with CNC machining. The radiation characteristics are measured, and for both polarizations, suppression of  $-28$  dB side lobe level has been achieved with a 1.2 m diameter main reflector.

## 1. INTRODUCTION

Meteorological forecasting has always been important; therefore, with the advance of technologies, more and more sophisticated measurement systems have been developed. Today, radar technologies [1] are unavoidable in weather forecasts. Recently, the electronic and signal processing of meteorological radars has been tremendously improved; however, the utilized antennas do not follow this trend. For example, to distinguish rain and hail polarimetric radio units can be utilized where low side lobe level (SLL) and high cross polarization isolated antennas are required. Parabolic antennas are widely used in weather radar applications because of their high power handling capabilities, high efficiency, cylindrical symmetric radiation pattern, and relatively simple mechanical structure compared to arrays with identical aperture. Several methods have been investigated that focus on SLL suppression of parabolic antennas. Theoretical illumination patterns have been studied [8] to decrease side lobe levels. The phase cancellation principle to suppress certain side lobes has been applied by attaching plates to reflector surface [9] or by adding an additional rim to the edge of a parabolic shaped main reflector [13]. Other solutions resulted in nonparabolic reflectors [9]; however, these designs can lead to a complicated fabrication process. During the last decade, metamaterial technologies have been considerably improved and allow the engineering of antenna parameters including radiation pattern. Cylindrically symmetric periodic structures have been utilized as subreflectors [2–4, 12] to enhance different electromagnetic properties.

In this paper, a novel subreflector with cylindrical symmetry is introduced. The developed structure is self-supporting, which is a subreflector without holding struts. The self-

supporting configuration allows us to keep the antenna efficiency high. It maintains the cylindrical symmetry of the radiation pattern, and at the same time makes fabrication easier. The previously developed subreflectors have considerable side lobe levels [3, 4] due to diffraction effects at the edge of the main reflectors compared to the prime focal configurations [8]. The geometry of our subreflector is optimized to achieve satisfactory edge illumination levels and consequently low side lobes.

The paper is organized as follows. Section 2 presents the analytical formulas deduced for the design of a low side-lobe parabolic antenna. The desired radiation pattern is also deduced in analytic form, which will serve as a reference in the objective function of a full-wave optimization to determine the geometry of the corrugations. The details of the design procedure are presented. In section 3, the fabricated samples are shown, and the measurement configuration is described. Measured and calculated illumination and radiation patterns are also compared. In section 4, a comparison between other works and our design is provided. The details of the analytical derivations can be found in the appendix.

## 2. ANTENNA DESIGN AND SIMULATION

Different types of feed configurations can be utilized to illuminate parabolic reflectors. In prime focus configurations, a corrugated feed is placed at the focal point of the main reflector. To further enhance the characteristic of the antenna, subreflectors can also be utilized. The geometrical configuration of the designed meteorological antenna is shown in Figure 1(a). The subreflector is mounted on the main reflector with a circular feeding waveguide. The geometry of the subreflector is also cylindrically symmetric; therefore, its fabrication is relatively simple with standard computer numerical control (CNC)

\* Corresponding author: Zsolt Szabó (szabo.zsolt@itk.ppke.hu).

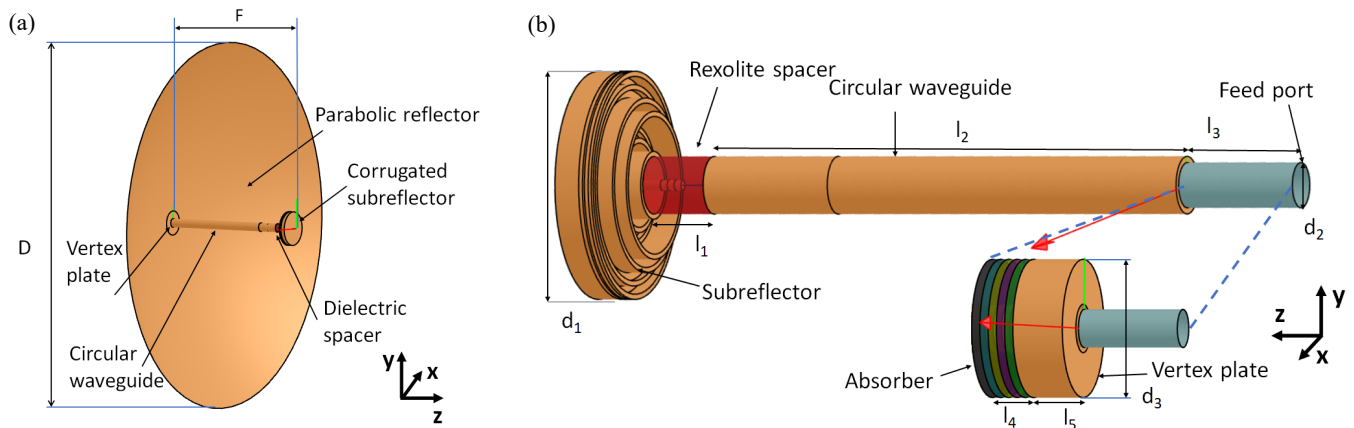


**FIGURE 1.** The geometry of the meteorological antenna. (a) Parabolic antenna with the designed subreflector. (b) The geometry of the subreflector. The orange parts are made from aluminium, the red part is made from dielectric (Rexolite). The inset shows the vertex plate covered with absorbing material for anechoic chamber measurements.

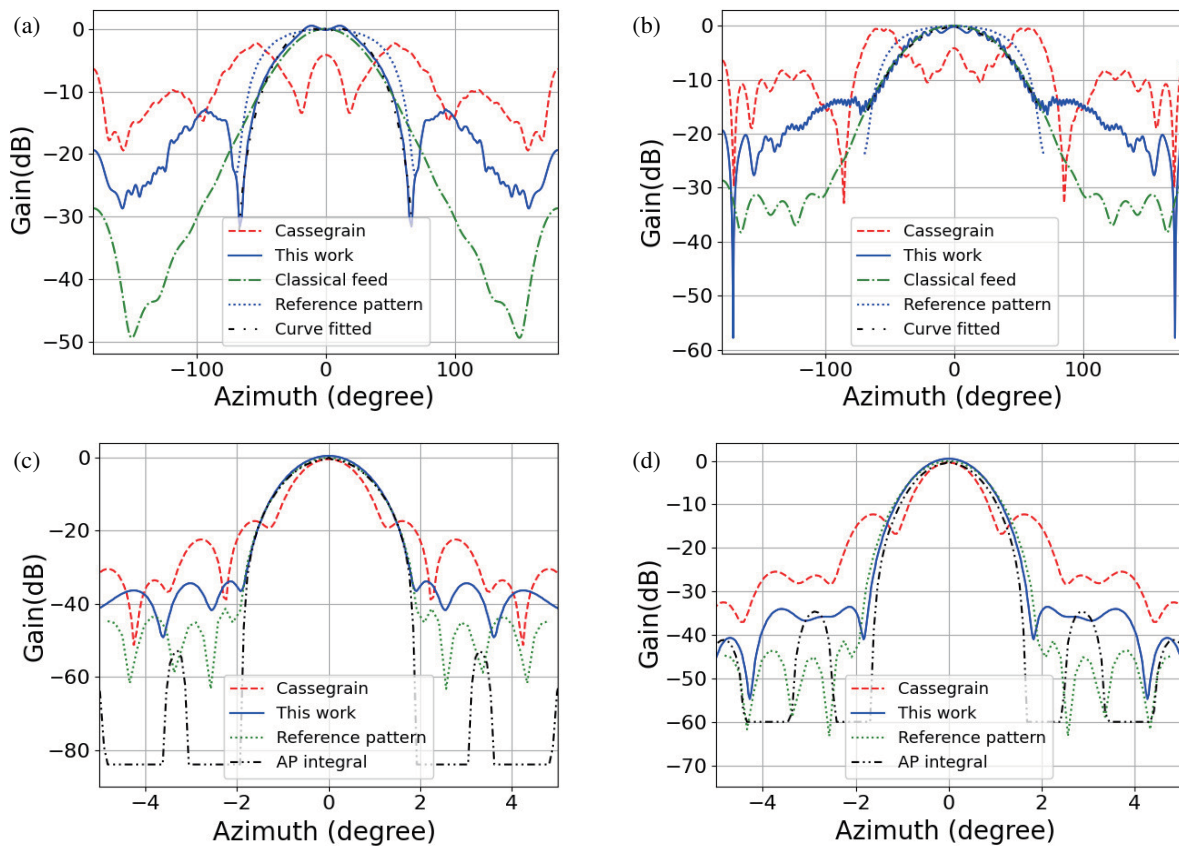


**FIGURE 2.** Comparison of illumination and radiation patterns for different parabolic antenna configurations (a) illumination patterns in horizontal polarization ( $xoz$ -plane), (b) illumination patterns in vertical polarization ( $yoz$ -plane), (c) radiation patterns in horizontal polarization ( $xoz$ -plane), (d) radiation patterns in vertical polarization ( $yoz$ -plane).

machining, and the radiation pattern is symmetric as well. The main goal is to design the geometry of the subreflector, which has improved side lobe-level suppression. As the first step of the design, a proper illumination pattern is selected, based on closed-form expressions and curve fittings of full-wave electromagnetic simulations. Novel analytical expressions of aperture integrals are deduced, which can have an important role

in the general design of parabolic antennas. The initial geometry of the subreflector is chosen with corrugation depths of  $\lambda/4$ , which is further optimized to provide similar illumination patterns as the previously deduced reference analytical expressions.

During the design procedure, two main reflector geometries have been considered with parabolic reflector diameters

of  $D = 1.2$  m and  $D = 1.8$  m, while keeping the focal length  $F$  to diameter ratio constant  $F/D = 0.375$ . Applying basic trigonometry, the edge illumination angle  $\theta_{illumax}$  can be calculated as

$$\theta_{illumax} = \tan^{-1} \left( \frac{r_{refl}}{F - \frac{r_{refl}^2}{4F}} \right) = 67.4^\circ, \quad (1)$$

where  $r_{refl} = D/2$  is the main reflector radius. The illumination pattern of the subreflector will exhibit its first null at the angle

$$\theta = \sin^{-1} \left( \frac{u\lambda}{2\pi r_{refl}} \right), \quad (2)$$

where  $u$  is the angular parameter of the parabolic reflector. This formula will be utilized to obtain the value of  $u$  for a given angle  $\theta$ .

### 2.1. Initial Antenna Illumination Calculations

The illumination pattern  $f(r)$  of the prime focal configurations can be expressed in the form of the following analytical expression [8]

$$f(r) = \frac{1}{3} + \frac{2J_0(3.8325r)}{3}, \quad (3)$$

where  $r$  is the relative radius of the aperture, and  $J_0$  is the zero-order Bessel function. The corresponding radiation pattern  $F_3(u)$  can be expressed as

$$F_3(u) = \frac{6J_1(u)}{11u} + \frac{288J_3(u)}{11u^3} + \frac{768J_4(u)}{11u^4}, \quad (4)$$

where  $u$  is the angular parameter,  $J_1$  the first order,  $J_3$  the third order, and  $J_4$  the fourth-order Bessel function. The angular parameter has been selected in the range of  $[-50, 50]$  to produce the radiation pattern in the  $[-12^\circ, 12^\circ]$  angular range. With this expression side lobe levels below  $-40$  dB can be achieved. To validate these expressions, a conical horn antenna with five corrugations has been designed with the commercial TICRA-Champ electromagnetic solver. In Figures 2(a) and (b), the illumination pattern of (3) is compared to the conical horn, and a good match can be observed between the characteristics. For analytical expression (4), the side lobe levels are below  $-40$  dB due to the proper edge illumination at  $67.4^\circ$  as can be observed in Figures 2(c) and (d).

### 2.2. Novel Design Equations for Self-Supporting Parabolic Antenna Configurations

The illumination pattern described with (3) is not suitable for self-supporting subreflector design; therefore, novel equations have been deduced for both polarizations. The deduced analytical expressions have relatively simple form and contain only Bessel functions, and the details of the derivations can be found in the appendix. For horizontal polarization, the illumination pattern can be expressed as

$$f_h(r) = 0.258 + \frac{2J_0(4.2r)}{3} + 0.6J_1(3.3r) - J_2(r), \quad (5)$$

where  $r$  is the relative radius, and  $J_2$  is the second-order Bessel function. For vertical polarization, the illumination pattern can be written as

$$f_v(r) = 0.3 + \frac{2J_0(3r)}{3} + \frac{J_2(r)}{3}. \quad (6)$$

The calculated illumination patterns are presented with gray dashed lines in Figures 2(a) and (b). Analytical solutions for the radiation pattern  $F(u)$  have also been deduced by evaluating the unperturbed aperture integral [10]

$$F(u) = \int_0^1 f(r)J_0(ur)rdr, \quad (7)$$

where  $f(r)$  is the illumination pattern for horizontal or vertical illuminations. The range of the integration is limited to the interval  $[0, 1]$ , which is equivalent to the illumination range of the main reflectors of  $[0, 67.4]^\circ$ . After mathematical manipulations (for more details see the appendix), the radiation pattern for horizontal polarization  $F_h(u)$  can be written as

$$\begin{aligned} F_h(u) &= 0.258 \frac{J_1(u)}{u} \\ &+ \frac{2}{3} \frac{4.2J_1(4.2)J_0(u) - uJ_0(4.2)J_1(u)}{17.64 - u^2} \\ &+ \frac{J_1(1)J_0(u) - uJ_0(1)J_1(u)}{1 - u^2} \\ &- 2 \sum_{h=0}^{\infty} \frac{(-1)^h}{h!(h+1)!} \left( \frac{1}{2} \right)^{2h+1} \left[ \frac{1}{u} r^{2h+1} J_1(ur) \right. \\ &\left. - \sum_{k=1}^h \frac{1}{u^{k+1}} \prod_{p=0}^{k-1} 2(h-p) r^{2h-k+1} J_{k+1}(ur) \right] \\ &- 0.6 \sum_{h=0}^{\infty} \frac{(-1)^h}{h!(h+1)!} \left( \frac{3.3}{2} \right)^{2h+1} \left[ \frac{1}{u} r^{2h+1} J_1(ur) \right. \\ &\left. + \frac{1}{u^{2h+1}} (rJ_0(ur) + \Phi(ur)) \right. \\ &\left. - \sum_{k=1}^{h-0.5} \frac{1}{u^{k+1}} \prod_{p=0}^{k-1} 2(h-p) r^{2h-k+1} J_{k+1}(ur) - \right. \\ &\left. \sum_{k=h+0.5}^{2h} \frac{1}{u^{k+1}} \left\{ \prod_{p=0}^{h-0.5} 2(-h+p) \prod_{p=h+0.5}^{k-1} 2(2h-p-1) \right\} \right. \\ &\left. r^{2h-k+1} J_{2h-k}(ur) \right], \quad (8) \end{aligned}$$

and for the vertical polarization  $F_v(u)$  as

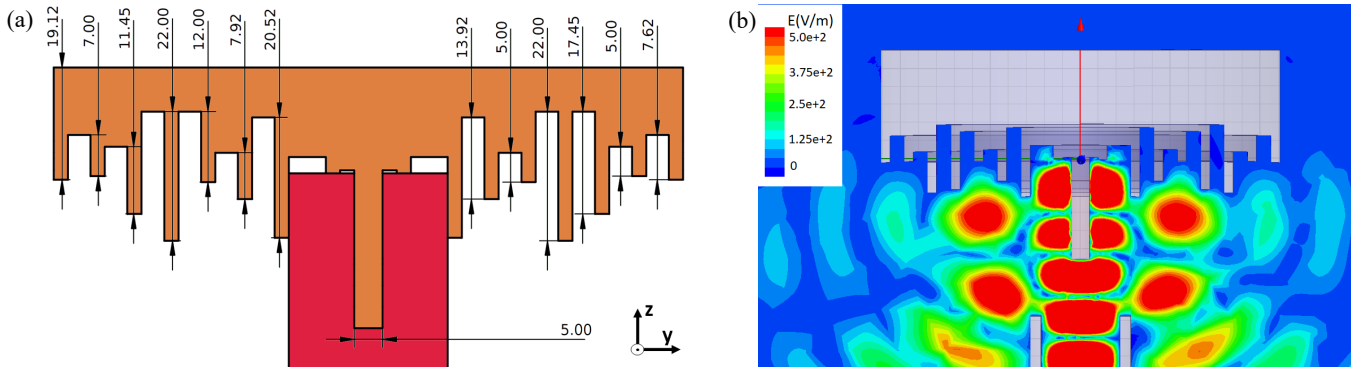


**FIGURE 3.** (a) Optimized geometry of the corrugated sub-reflector, where the orange part is made of aluminum and the red part is dielectric. (b) Distribution of the electric field after the insertion of the optimized corrugated parts.

$$F_v(u) = 0.3 \frac{J_1(u)}{u} + \frac{2}{3} \frac{3J_1(3)J_0(u) - uJ_0(3)J_1(u)}{9 - u^2} - \frac{1}{3} \frac{J_1(1)J_0(u) - uJ_0(1)J_1(u)}{1 - u^2} + \frac{2}{3} \sum_{h=0}^{\infty} \frac{(-1)^h}{h!(h+1)!} \left(\frac{1}{2}\right)^{2h+1} \left[ \frac{1}{u} r^{2h+1} J_1(ur) + \sum_{k=1}^h \frac{1}{u^{k+1}} \prod_{p=0}^{k-1} [-2(h-p)] r^{2h-k+1} J_{k+1}(ur) \right]. \quad (9)$$

With these formulas the radiation pattern can be calculated quickly as compared to numerical solvers. The source code of the aperture integral calculations can be downloaded from [21].

### 2.3. Numerical Simulation of the Subreflector

Cylindrical symmetric corrugated structures are known for their excellent pattern formation properties and are widely used in antenna engineering [15]. In [3], a corrugated subreflector with  $\lambda_0/4$  depth corrugations is presented. In [5], analytical expressions have been provided to design corrugated surfaces. The presented expressions are restricted to the  $\lambda_0/4$  corrugation depth; nevertheless, they are suitable for initial subreflector geometry calculations. Our design, which is shown in Figure 1(b), is an aluminum cylinder with non-resonant corrugation insets. The overall structure is held in place with a dielectric spacer made of Rexolite 1422. For the numerical design of the subreflector geometry, two electromagnetic solvers, which complement each other and are based on different numerical methods, have been selected. TICRA-Champ [17] is a method of moments software, which is extremely efficient in solving cylindrical symmetry electromagnetic problems and is also equipped with efficient optimization routines. This software provides the optimized geometry of the subreflector and the current distributions. The obtained geometry is verified with the finite element solver Ansys-HFSS, which is also utilized to calculate the electric and magnetic field distribution of the entire meteorological antenna. The geometry of the subreflector is shown in Figure 1(b), where the orange parts are made from aluminum, and the red part is made from dielectric (Rexolite 1422). The feeding circular waveguide is plotted in green. The subreflector is excited with  $TE_{11}$  mode through the cylindrical waveguide

port. The cylindrical waveguide is impedance matched with a stepped dielectric transition.  $TE_{11}$  is converted to the  $HE_{11}$  waveguide mode due to the presence of the Rexolite dielectric spacer. After exiting the dielectric spacer, the  $HE_{11}$  mode is converted into two dominant TEM modes. The modes of the corrugated surface are excited with the use of a short circuit cap [3] and with the insertion of a tuning screw.

The initial corrugation with depths  $\lambda/4$  is optimized using the One-sided Least Squares (OSLS) and MinMax optimization techniques of the TICRA software. To reduce computational time, optimization is performed without the main reflector. The deduced analytical illumination patterns (5) and (6) have been used as the goal of the objective function, resulting in a significant reduction in optimization time. The resulting optimized geometry and electric field distribution are shown in Figures 3(a) and (b). The illumination patterns of the optimized subreflector calculated with full wave electromagnetic solver are shown in Figure 4 and agree well with the analytically defined ones; both have an edge taper bellow  $-20$  dB. The simulations have been performed for 1.2 m and 1.8 m diameter main reflectors. In the case of the dish with 1.2 m diameter, the side lobe levels for both polarizations deteriorate by 3 dB, but the absolute value of the side lobe levels remains unchanged. Therefore, we have concluded that the side lobe level is attributed to diffracted rays caused by the subreflector and by the supporting cylindrical waveguide itself.

### 3. FABRICATION AND MEASUREMENT

The optimized subreflector has been fabricated with CNC machining. The fabricated parts are shown in Figure 5(a). Measurements were taken in an anechoic chamber and at open field test site.

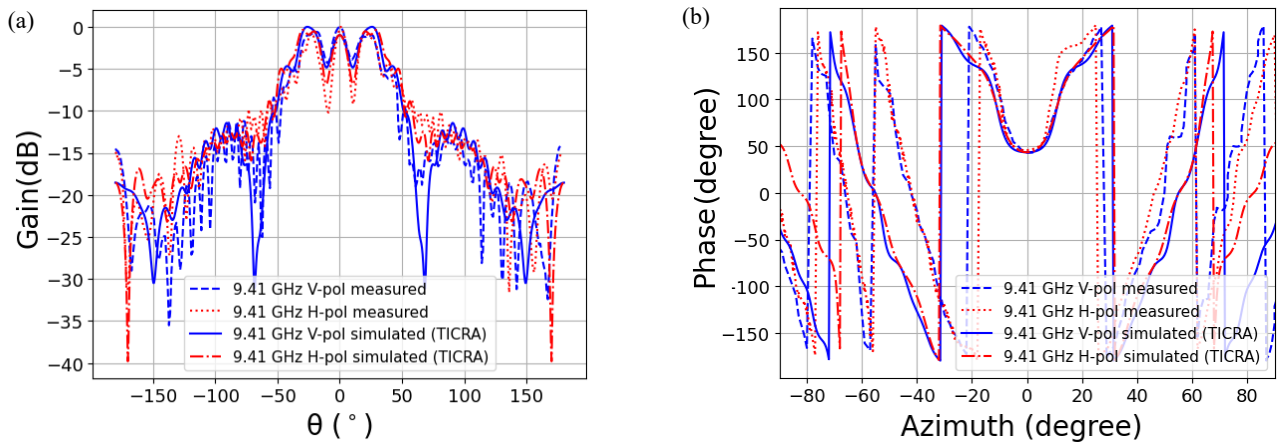


FIGURE 4. Illumination patterns of the subreflector at 9.41 GHz. (a) Amplitude. (b) Phase.

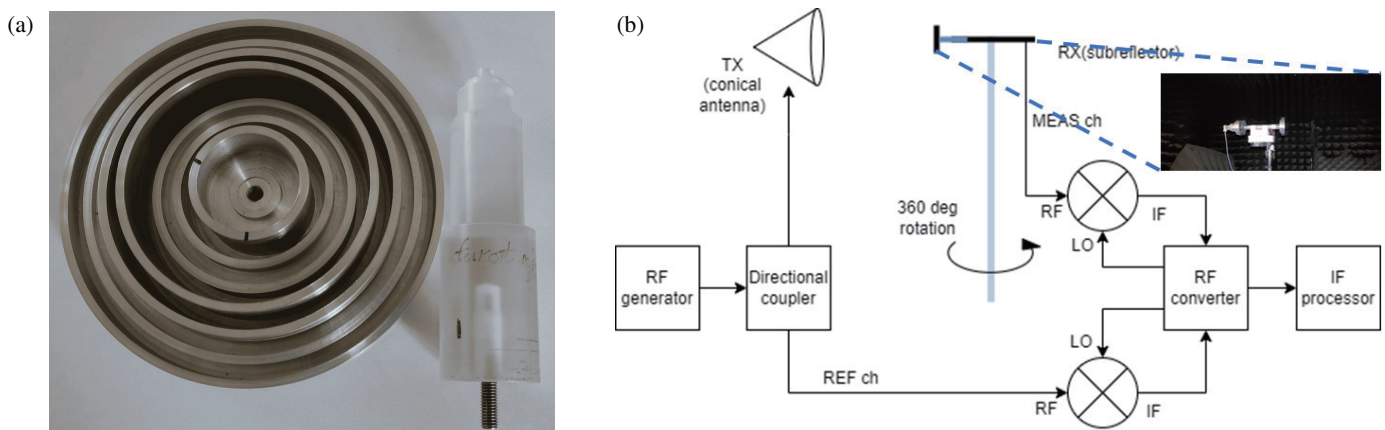


FIGURE 5. (a) Manufactured components: left-subreflector, right-dielectric spacer. (b) The configuration of the anechoic chamber measurement.

### 3.1. Measurement of the Illumination Pattern

The illumination patterns of the subreflector have been measured in an anechoic chamber with the instrumentation setup presented in Figure 5(b). Due to mechanical fixation an auxiliary 30 mm thick aluminium cylinder is applied, which is covered with an additional ABS-LCF-25 absorber to mitigate its electromagnetic effects. In simulations, the absorbing material is modelled as a five layer graded index material, and the geometry is shown in the inset in Figure 1(b). During normal operation, the vertex plate has no effect on the radiation pattern. The measured amplitude and phase characteristics have been compared with the numerically calculated ones, and good agreement can be observed as shown in Figures 4(a) and (b), where the  $H$  polarization is in the  $xoz$  plane and  $V$  polarization in the  $yoz$  plane. In spite of all previous efforts, small deviations can be observed between the measured and simulated results. The differences are presumably caused by the imperfections of our anechoic chamber. For vertical polarization, the following correction angles [9.38 GHz:  $107^\circ$ , 9.41 GHz:  $-118^\circ$ , 9.44 GHz:  $0^\circ$ ], while in the case of horizontal polarization [9.38 GHz:  $204^\circ$ , 9.41 GHz:  $-13^\circ$ , 9.44 GHz:  $80^\circ$ ] angles have been applied.

### 3.2. Measurement of the Radiation Pattern

The measurements of the fully mounted meteorological antenna, which includes the main reflector of 1.2 m diameter and the optimized subreflector, are performed at open field test site to satisfy the far-field conditions, which cannot be reached in the anechoic chamber. At the transmitter side, a 1.2 m diameter parabolic antenna is placed 6 m above the physical ground. In order to facilitate the radiation pattern measurement, the meteorological antenna is mounted onto the top of a 55 meter high measurement tower, which can be rotated and tilted. The measured radiation patterns at midband (9.41 GHz) are presented in Figures 6(a) and (b), where close agreement with the simulated results can be observed. The measured side lobe levels are 2 dB above the simulated ones, which can be attributed to the surface accuracy of the main reflector and off axis alignment of the subreflector. The small ripples in the measured radiation patterns are due to the windy environment.

## 4. COMPARISON WITH OTHER PARABOLIC ANTENNA DESIGNS

In Table 1 the performances of several parabolic antennas equipped with self-supporting subreflectors are compared. The

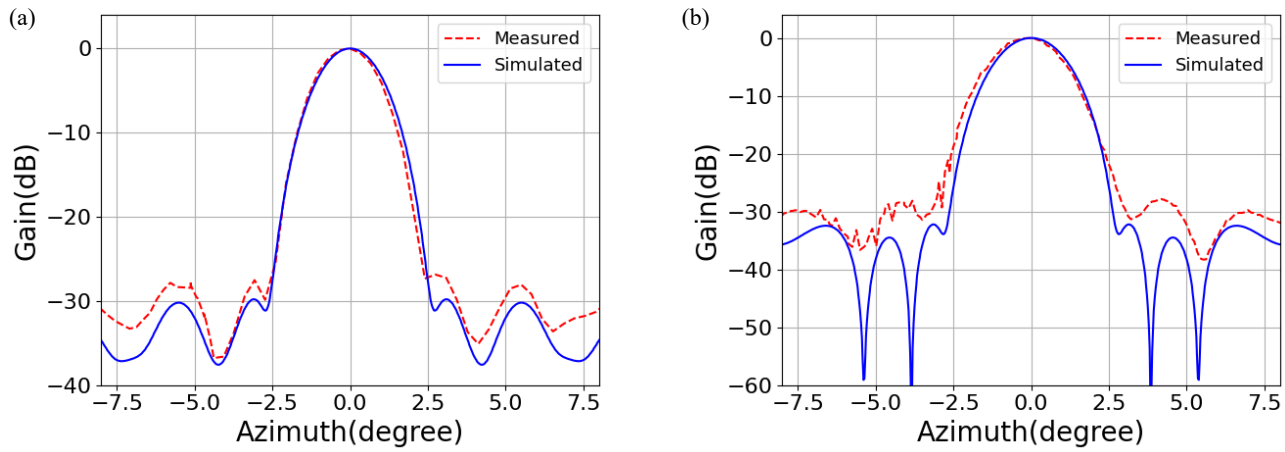


**FIGURE 6.** Measured and simulated radiation patterns of the fully mounted meteorologic antenna at 9.41 GHz (midband), (a) Horizontal polarization ( $xoz$ -plane), (b) Vertical polarization ( $yoz$ -plane). The measurements are performed at open field test site to satisfy the far-field conditions.

**TABLE 1.** Comparison with other parabolic antennas.

| Reference | $f$ (GHz)      | Diameter (m) | Gain (dBi)      | SLL (dB)            | Efficiency (%) |
|-----------|----------------|--------------|-----------------|---------------------|----------------|
| [3]       | 12             | 1            | 40              | -15                 | 65             |
| [4]       | 30.4           | 0.43         | 39.6            | -23                 | 53             |
| [16]      | 27/29/31       | NA           | NA              | NA                  | 57/69/72       |
| [18]      | 5.7            | 0.46/0.61    | 25/27.5         | < -20               | 43/43          |
| [19]      | 5.2/5.5/5.8    | 0.9          | 30.6/30.2/31.2  | -24.8/ -17.8/ -14.6 | 48/39/49       |
| TW        | 9.38/9.41/9.44 | 1.2          | 38.3/38.45/38.6 | < -28               | 50/49/53       |

table presents the antenna gain at different operating frequencies and different dish sizes. These gains are only indicative and cannot provide a fair comparison between the designs. However, the efficiencies  $\epsilon_{ant}$  and  $\epsilon_{ant}(dB)$ , which can be calculated as

$$\epsilon_{ant} = 10^{\frac{1}{10}} + 10^{\epsilon_{ant}(dB)}, \quad (10)$$

$$G_{100} = 20 \log \frac{D\pi}{\lambda}, \quad (11)$$

where  $G_{100}$  is the maximum gain of 100%, are more suitable for comparing the performance of the antennas. Note that these efficiencies are not provided in all references, but they are calculated in this work. The table contains the worst-case scenarios because this is what defines the usability of the particular design.

## 5. CONCLUSION

The presented design procedure can achieve suppressed side lobe levels in parabolic antenna configurations with self-supporting subreflector. The deduced mathematical expressions are general. They can significantly reduce the simulation time and provide knowledge about the radiation patterns in an analytical way. The designed self-supporting subreflector has been fabricated and characterized in an anechoic chamber. The radiation characteristics of the fully mounted meteorological antenna have been measured at open

field test site to meet the far-field conditions. Based on the measured data and a comparison with other published designs, it can be concluded that our design has superior side lobe level suppression. Side lobe levels may be further improved by decreasing the reflection caused by the cylindrical waveguide surface and the diffraction caused by the subreflector edge.

## ACKNOWLEDGEMENT

This work was funded by the National Research, Development and Innovation Office of Hungary (NKFIH) under Grant K-132050. We thank Grante Co. for manufacturing the subreflectors and providing the measurement site and instrumentation.

## APPENDIX A. ANALYTICAL SOLUTION FOR APERTURE INTEGRAL

In this section, the analytical solution of the aperture integral for the horizontal polarization is presented. The illumination function for horizontal polarization (5) has been substituted into the aperture integral (7), which can be written as

$$F_h(u) = 0.258 \int_0^1 r J_0(ur) dr + \frac{2}{3} \int_0^1 r J_0(4.2r) J_0(ur) dr + 0.6 \int_0^1 r J_1(3.3r) J_0(ur) dr - \int_0^1 r J_2(r) J_0(ur) dr. \quad (A1)$$

The first two terms of (A1) have a direct analytical solution

$$0.258 \int_0^1 r J_0(ur) dr = 0.258 \frac{J_1(u)}{u}, \quad (A2)$$

and

$$\begin{aligned} & \frac{2}{3} \int_0^1 r J_0(4.2r) J_0(ur) dr \\ &= \frac{2}{3} \frac{4.2 J_1(4.2) J_0(u) - u J_0(4.2) J_1(u)}{17.64 - u^2}, \quad (A3) \end{aligned}$$

where the singularity at  $u = 4.2$  can be eliminated by numerical interpolation. There is no direct analytical solution for the third and fourth terms of (A1). Nevertheless, analytical expressions can be obtained by using the power series representation of the Bessel functions and by applying integration rules [20]. The first-order Bessel function can be expressed as

$$J_1(\alpha r) = \sum_{h=0}^{\infty} \frac{(-1)^h}{h!(h+1)!} \left(\frac{1}{2}\right)^{2h+1} \alpha^{2h+1} r^{2h+1}. \quad (A4)$$

To solve integrals of  $\int_0^1 J_0(r) dr$  type the Struve function  $H_v(r)$ , which is defined as

$$H_v(\alpha r) = \sum_{h=0}^{\infty} \frac{(-1)^h}{(h+0.5)!(h+v+0.5)!} \left(\frac{1}{2}\right)^{2h} \alpha^{2h} r^{2h}, \quad (A5)$$

can be utilized in the following way

$$\Phi(r) = \frac{\pi r}{2} [J_1(r)H_0(r) - J_0(r)H_1(r)], \quad (A6)$$

where  $\Phi$  is a correction factor. Integrals of type  $\int_0^1 r^m J_n(r) dr$  can be solved by applying the following two relations [15]

$$\begin{aligned} & \int_0^1 r^m J_n(r) dr \\ &= r^m J_{n+1}(r) - (m-n-1) \int_0^1 r^{m-1} J_{n+1}(r) dr, \quad (A7) \end{aligned}$$

$$\begin{aligned} & \int_0^1 r^m J_n(r) dr \\ &= -r^m J_{n-1}(r) + (m+n-1) \int_0^1 r^{m-1} J_{n-1}(r) dr. \quad (A8) \end{aligned}$$

The integrals with Bessel functions whose coefficient contains multiplication by an additional constant  $u$  can be solved with the following relations

$$\begin{aligned} \int r^{m+1} J_n(ur) dr &= \frac{1}{u} r^{m+1} J_{n+1}(ur) + C, \\ \int r^{m-1} J_n(ur) dr &= -\frac{1}{u} r^{1-m} J_{n-1}(ur) + C. \quad (A9) \end{aligned}$$

With the combination of these relations, we have deduced the following analytical expressions

$$\begin{aligned} \int_0^1 r^m J_0(ur) dr &= \frac{1}{u} r^m J_1(ur) + \frac{1}{u^m} (r J_0(ur) + \Phi(ur)) \\ &+ \sum_{k=1}^{\frac{m}{2}-1} \frac{1}{u^{k+1}} \prod_{p=0}^{k-1} [-(m-2p-1)] r^{m-k} J_{k+1}(ur) \\ &+ \sum_{k=\frac{m}{2}}^{m-1} -\frac{1}{u^{k+1}} \prod_{p=0}^{\frac{m}{2}-1} [-(m-2p-1)] \\ &\prod_{p=\frac{m}{2}}^{k-1} [(2m-2p-1)] r^{m-k} J_{m-k-1}(ur), \quad (A10) \end{aligned}$$

where  $m$  is an even integer, and

$$\begin{aligned} \int_0^1 r^m J_0(ur) dr &= \frac{1}{u} r^m J_1(ur) \\ &+ \sum_{k=1}^{\frac{m-1}{2}} \frac{1}{u^{k+1}} \prod_{p=0}^{k-1} (-m+2p+1) r^{m-k} J_{k+1}(ur), \quad (A11) \end{aligned}$$

where  $m$  is an odd integer. The previous formula for even  $m$  values has been substituted into the third term of (A1), and after setting the coefficient  $\alpha = 3.3$  it can be expressed analytically as

$$\begin{aligned} & 0.6 \int_0^1 r J_1(3.3r) J_0(ur) dr \\ &= 0.6 \int_0^1 r \sum_{h=0}^{\infty} \frac{(-1)^h}{h!(h+1)!} \left(\frac{3.3r}{2}\right)^{2h+1} J_0(ur) dr \\ &= 0.6 \sum_{h=0}^{\infty} \frac{(-1)^h}{h!(h+1)!} \left(\frac{3.3}{2}\right)^{2h+1} \\ &\left[ \frac{1}{u} r^{2h+1} J_1(ur) + \frac{1}{u^{2h+1}} (r J_0(ur) + \Phi(ur)) - \right. \\ &\sum_{k=1}^{h-0.5} \frac{1}{u^{k+1}} \prod_{p=0}^{k-1} 2(h-p) r^{2h-k+1} J_{k+1}(ur) - \\ &\left. \sum_{k=h+0.5}^{2h} \frac{1}{u^{k+1}} \left\{ \prod_{p=0}^{h-0.5} 2(-h+p) \prod_{p=h+0.5}^{k-1} 2(2h-p-1) \right\} \right. \\ &\left. r^{2h-k+1} J_{2h-k}(ur) \right]. \quad (A12) \end{aligned}$$

The solutions involving Struve functions exist only for zero-order Bessel functions. Therefore, in our formulation reverse indexing has been applied, which starts from the  $m/2$  index.

The fourth term of (A1) can be divided into two parts by applying Bessel's recurrence relation

$$\int_0^1 r J_2(r) J_0(ur) dr$$

$$= \int_0^1 [-rJ_0(r)J_0(ur) + 2J_1(r)J_0(ur)] dr, \quad (\text{A13})$$

where the first term can be calculated directly using the following relation

$$\int_0^1 rJ_0(r)J_0(ur)dr = \frac{J_1(1)J_0(u) - uJ_0(1)J_1(u)}{1 - u^2}. \quad (\text{A14})$$

The second term is not solvable directly. Therefore, we have utilized the power series representation of the first order Bessel function (A4) with  $\alpha = 1$ ; then the integration can be solved for different powers individually, and the analytical solution can be written as

$$2 \int_0^1 J_1(r)J_0(ur)dr = 2 \int_0^1 \sum_{h=0}^{\infty} \frac{(-1)^h}{h!(h+1)!} \left(\frac{r}{2}\right)^{2h+1} J_0(ur)dr = 2 \sum_{h=0}^{\infty} \frac{(-1)^h}{h!(h+1)!} \left(\frac{1}{2}\right)^{2h+1} \left[ \frac{1}{u} r^{2h+1} J_1(ur) + \sum_{k=1}^h \frac{1}{u^{k+1}} \prod_{p=0}^{k-1} 2(-h+p)r^{2h-k+1} J_{k+1}(ur) \right]. \quad (\text{A15})$$

Collecting these results the radiation pattern (8) for horizontal polarization is obtained. A similar derivation, which involves only integrals with analytical expression already presented, leads to the radiation pattern for vertical polarization (9). The presented analytical expressions of the aperture integrals have been verified with numerical integration.

## REFERENCES

- [1] Vasquez, T., *Weather Radar Handbook*, Weather Graphics Technologies, 2015.
- [2] Kildal, P. S., "Artificially soft and hard surfaces in electromagnetics," *IEEE Transactions on Antennas and Propagation*, Vol. 38, No. 10, 1537–1544, Oct. 1990.
- [3] Kildal, P. S., "The hat feed — A dual-mode rear-radiating waveguide antenna having low cross polarization," *IEEE Transactions on Antennas and Propagation*, Vol. 35, No. 9, 1010–1016, Sep. 1987.
- [4] Hansen, J., A. A. Kishk, P. S. Kildal, and O. Dahlsjo, "High performance reflector hat antenna with very low sidelobes for radio-link applications," in *IEEE Antennas and Propagation Society International Symposium*, Vol. 2, 893–896, Newport Beach, CA, USA, 1995.
- [5] Albani, M., P. Piazzesi, F. Capolino, S. Maci, and R. Tiberio, "Shielding effect of a thick screen with corrugations," *IEEE Transactions on Electromagnetic Compatibility*, Vol. 40, No. 3, 235–239, Aug. 1998.
- [6] Rajo-Iglesias, E., O. Quevedo-Teruel, and L. Inclan-Sanchez, "Planar soft surfaces and their application to mutual coupling reduction," *IEEE Transactions on Antennas and Propagation*, Vol. 57, No. 12, 3852–3859, Dec. 2009.
- [7] Kwon, D.-H., "Modulated reactance surfaces for leaky-wave radiation based on complete aperture field synthesis," *IEEE Transactions on Antennas and Propagation*, Vol. 68, No. 7, 5463–5477, Jul. 2020.
- [8] Yampol'skiy, V. G., Q.-T. O., and I.-S. L., "Antenny i EMS," *Radio i Svyaz*, 54–56, 1983.
- [9] Collin, R. E. and G. L., R., "Low sidelobe level low-cost earth station antennas for the 12 GHz broadcasting satellite service," *NASA-CR-159703*, 1979.
- [10] Cornbleet, S., *Microwave Optics*, Academic Press, 1976.
- [11] Asci, Y., E. Curuk, K. Yegin, and C. Ozdemir, "Improved splash-plate feed parabolic reflector antenna for Ka-band VSAT applications," in *2016 46th European Microwave Conference (EUMC)*, 1283–1286, London, England, Oct. 2016.
- [12] Yousefnia, M., P. A., and H. M., "Analysis and design of parabolic hat feed antenna," Vol. 3A, 650–653, Washington, DC, USA, 2005.
- [13] Ellingson, S. and R. Sengupta, "Sidelobe modification for reflector antennas by electronically reconfigurable rim scattering," *IEEE Antennas and Wireless Propagation Letters*, Vol. 20, No. 6, 1083–1087, Jun. 2021.
- [14] Clarricoats, P. J. B. and O. A., D., "Corrugated horns for microwave antennas," in *IEE Electromagnetic Waves Series*, Peter Peregrinus, 1984.
- [15] Balanis, C. A., *Antenna Engineering*, John Wiley and Sons, 2005.
- [16] Yang, J. and P. Kildal, "FDTD design of a chinese hat feed tor shallow mm-wave reflector antennas," in *IEEE Antennas and Propagation Society International Symposium — Antennas: Gateways to The Global Network*, Vol. 4, 2046–2049, Atlanta, GA, USA, Jun. 1998.
- [17] Viskum, H.-H., "CHAMP — the dedicated design tool for rotationally symmetric horns and reflector terminals," in *2013 IEEE Antennas and Propagation Society International Symposium (apsursi)*, 2325–2326, Orlando, FL, USA, Jul. 2013.
- [18] Kishk, A. and L. Shafai, "Small reflector antenna with low sidelobes," *IEEE Transactions on Antennas and Propagation*, Vol. 51, No. 10, 2, 2907–2912, Oct. 2003.
- [19] Olszewska, M. and W. Gwarek, "A dual reflector antenna for point-to-point system applications," in *18th International Conference on Microwaves, Radar and Wireless Communications (MIKON-2010)*, 1–4, Radar and Wireless Communications (mikon), Vilnius, Jun. 2010.
- [20] Abramowitz, M. and S. I., *Handbook of Mathematical Functions: With Formulas, Graphs, and Mathematical Tables*, Dover Publications, 1965.
- [21] Code to calculate the aperture integral. [Online]. Available: <https://bitbucket.org/eszesandras/ais> [accessed 12-September-2023].